Journal of the Optical Society of America B
OPTICAL PHYSICS

Preserving nonclassical correlations in strongly unbalanced conditions

A. Allevi[1,2,*] and M. Bondani[2]

[1]Department of Science and High Technology, University of Insubria, Via Valleggio 11, I-22100 Como, CO, Italy
[2]Institute for Photonics and Nanotechnologies, CNR, Via Valleggio 11, I-22100 Como, CO, Italy
*Corresponding author: alessia.allevi@uninsubria.it

Received 28 June 2019; revised 7 October 2019; accepted 9 October 2019; posted 9 October 2019 (Doc. ID 371259); published 11 November 2019

It is well known that optical losses represent the main obstacle to the real exploitation of quantum optical systems for quantum technology. Here we investigate to what extent the presence of unbalanced losses between the two parties of a mesoscopic twin-beam state can prevent or not the observation of nonclassical correlations. Moreover, we focus on the survival of nonclassicality in the presence of asymmetric lossy channels modeled according to specific statistical distributions.

https://doi.org/10.1364/JOSAB.36.003275

1. INTRODUCTION

Quantum states of light represent a useful tool for coding and transmitting information. Indeed, in the last 15 years many experimental implementations on very different scales and through different media [1–13] have demonstrated that quantum light can be successfully used for secure data transfer [14]. Despite these local realizations, the main obstacle to the development of a global communication network is still given by the presence of noise sources in the communication channels. For instance, the communications based on the atmospheric link are limited by the turbulent variations, both in time and space, of the optical properties of the atmosphere [15]. In many cases, the most detrimental drawback is given by losses [16], which irreversibly modify the statistical properties of nonclassical states of light thus making the observation of their nonclassical nature hard or even impossible [17].

Moreover, if the quantum resource is embedded in a multipartite system, the presence of losses can affect differently its components. For instance, in the case of bipartite entangled states, an unbalanced collection of the two parties could prevent the observation of nonclassical correlations [18]. For the practical exploitation of quantum states bearing asymmetric amounts of losses, investigating to what extent their nonclassical nature can survive is thus highly desirable.

In this paper, we consider a mesoscopic twin-beam (TWB) state in which the two parties are affected by different amounts of loss: on one arm we assume fixed losses, while on the other arm we change them according to a specific statistical distribution. We notice that the use of TWB states to prove the robustness of quantum resources propagating in lossy channels is equivalent to the employment of maximally entangled states, as already demonstrated in [19]. First of all, we show the conditions under which the existence of an imbalance between the two parties of a TWB state is detrimental for the observation of nonclassical correlations. In particular, we demonstrate that this effect is more evident at increasing number of photons per mode. Second, we model the varying amount of loss on one arm according to some specific statistical distributions in order to simulate the propagation through more realistic media. In more detail, we consider a uniform distribution, a Gaussian distribution, and a log-normal distribution. We prove that, even in the presence of strong imbalance, there are conditions in which it is still possible to observe nonclassicality.

Our work benefits of the use of photon-number-resolving (PNR) detectors, which allow us to perform measurements in the mesoscopic intensity domain, where the number of photons contained in each light pulse is in general larger than 1.

The paper is structured as follows: in Section 2 we discuss the role of the imbalance due to different amounts of loss in the two arms. We present both theoretical predictions and experimental observations. In Section 3, we model the loss on one arm according to specific distributions. Also in this case, we report on both theoretical and experimental results. In Section 4 we summarize our results and address future perspectives.

2. UNBALANCED DETECTION OF MESOSCOPIC STATES OF LIGHT

Let us consider a multi-mode TWB state $|\psi_\mu\rangle = \otimes_{k=1}^{\mu}|\psi\rangle_k$, in which all the μ modes are in the same state $|\psi\rangle_k = \sum_n \sqrt{(\langle\hat{n}\rangle^n/(1+\langle\hat{n}\rangle)^{n+1})}|n\rangle_k \otimes |n\rangle_k$ [20,21].

By assuming a pairwise generation of photons, the parties of the state $|\psi_\mu\rangle$ are characterized by a multi-mode thermal photon-number distribution:

$$p_n^\mu = \frac{(n+\mu-1)!}{n!(\mu-1)!(\langle n\rangle/\mu+1)^\mu(\mu/\langle n\rangle+1)^n}, \quad (1)$$

in which $\langle n\rangle$ is the total mean number of photons, while $\langle n\rangle/\mu$ is the mean number of photons per mode. In order to characterize the nonclassical correlations between the two parties, we consider the criterion based on the calculation of the noise reduction factor R, namely $R<1$. In terms of measurable quantities, that is of detected photons m, R is defined as

$$R = \frac{\sigma^2(m_1-m_2)}{\langle m_1\rangle+\langle m_2\rangle} = \frac{\langle (m_1-m_2)^2\rangle - \langle m_1-m_2\rangle^2}{\langle m_1\rangle+\langle m_2\rangle}, \quad (2)$$

where $\langle m_j\rangle = \eta_j\langle n\rangle$ is the mean number of photons in the j-th arm, η_j is the detection efficiency, and $\sigma^2(\cdot)$ is the variance. For the state $|\psi_\mu\rangle$ defined above, Eq. (2) can be expressed as

$$R = 1 - \frac{2\sqrt{\eta_1\eta_2}\sqrt{\langle m_1\rangle\langle m_2\rangle}}{\langle m_1\rangle+\langle m_2\rangle} + \frac{(\langle m_1\rangle-\langle m_2\rangle)^2}{\mu(\langle m_1\rangle+\langle m_2\rangle)}, \quad (3)$$

in which, to be general, we assume that each arm is characterized by a different value of quantum efficiency, i.e., $\eta_1\neq\eta_2$. Indeed, the third term on the right side of Eq. (3) takes into account the possible imbalance between the mean number of photons measured in the two arms. When $\eta_1=\eta_2=\eta$, this term is zero and Eq. (3) reduces to $R=1-\eta$, that is the lower bound fixed by the presence of a nonideal quantum efficiency in the detection process.

In order to better investigate the role of the imbalance between the two twin arms, in the following we assume that they are characterized by the same detection efficiency, η, and that one of the two arms, say the second one, is affected by an additional loss with respect to the other. Thus, by setting $\langle m_1\rangle = \eta_1\langle n\rangle \equiv \eta\langle n\rangle$ and $\langle m_2\rangle = \eta_2\langle n\rangle = \eta t\langle n\rangle$, Eq. (3) becomes

$$R(t) = 1 - \frac{2\eta t}{1+t} + \frac{(1-t)^2}{1+t}\frac{\langle m\rangle}{\mu}. \quad (4)$$

Note that the values of the factor t appearing in Eq. (4) are between 0 and 1. Thus t can be considered as a transmission efficiency characterizing only the second arm. By keeping the value of η fixed, it is interesting to investigate the behavior of R as a function of this transmission efficiency t for different choices of the number of photons per mode, $\langle m\rangle/\mu$. We note that a large value of $\langle m\rangle/\mu$ can be ascribed either to the generation of well-populated TWB states or to the production of few modes, down to a single one and vice versa. To make the point clearer, in Fig. 1 we plot R as a function of t for a typical value of η accessible with commercial PNR detectors and for some possible choices of $\langle m\rangle/\mu$. The general observation is that there is a threshold value of t, below which observing nonclassical correlations is not possible anymore. This threshold strongly depends on the value of $\langle m\rangle/\mu$ [22]. In particular, we note that the higher the mean number of photons for a fixed value of μ or the lower the number of modes for a fixed value of $\langle m\rangle$, the larger the value of R. This means that for multi-mode TWB states generated at a macroscopic intensity level even a small amount of imbalance in the detection chain can prevent the detection of sub-shot-noise correlations, even if their generation is perfectly pairwise. The same is true for low-intensity TWB states properly tailored to have only a single mode, such as those generated in nonlinear waveguides.

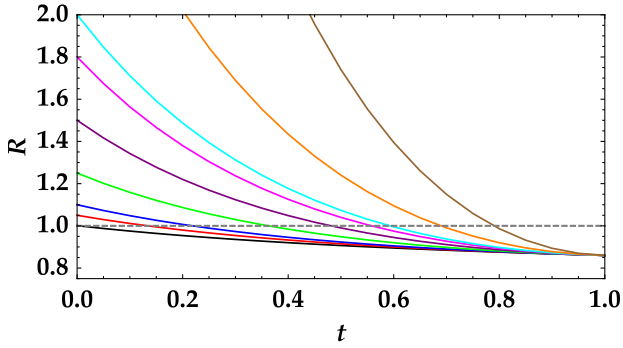

Fig. 1. Noise reduction factor R as a function of t for $\eta=0.14$, and different numbers of photon per mode. From bottom to top: $\langle m\rangle/\mu=0.001$ (black), 0.05 (red), 0.1 (blue), 0.25 (green), 0.5 (purple), 0.8 (magenta), 1 (cyan), 2 (orange), 5 (brown). The dashed gray line at $R=1$ represents the boundary condition between classicality and nonclassicality.

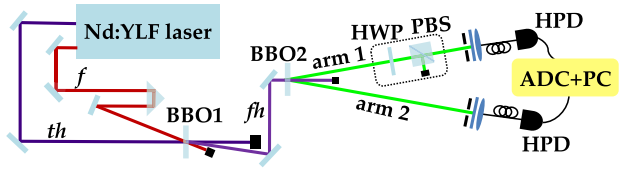

Fig. 2. Sketch of the experimental setup. The fourth-harmonic pulses (fh), produced in BBO1 by the nonlinear mixing of the fundamental (f) and the third-harmonic (th) fields of a Nd:YLF laser, are sent to BBO2 to produce parametric downconversion. Two twin portions at frequency degeneracy are selected by means of a proper spatial and spectral filtering, collected by two multi-mode fibers and sent to two hybrid photodetectors (HPDs). The outputs of the detectors are amplified, synchronously integrated, digitized, and acquired shot-by-shot (ADC + PC). The elements in the dashed rectangle, namely a half-wave plate (HWP) and a polarizing cube beam splitter (PBS), are used to change in a controlled way the light transmission in arm 1.

To experimentally verify this statement, in the following we present the experimental results obtained with a multi-mode TWB state at the mesoscopic intensity level. The experimental setup is sketched in Fig. 2. The fundamental (at 1047 nm) and third-harmonic (at 349 nm) fields of a Nd:YLF laser amplified at 500 Hz are sent to a β-barium-borate nonlinear crystal (BBO1, cut angle = 37°, 8 mm long) to produce the fourth-harmonic field (at 262 nm, 3.5 ps pulse duration) by noncollinear sum-frequency generation. This field pumps a parametric downconversion process in a second BBO crystal (BBO2, cut angle = 46.7°, 6 mm long). Two twin portions at frequency degeneracy (at 523 nm) are then spatially and spectrally selected by means of irises and interference filters. The collected light in each arm is then delivered to a PNR

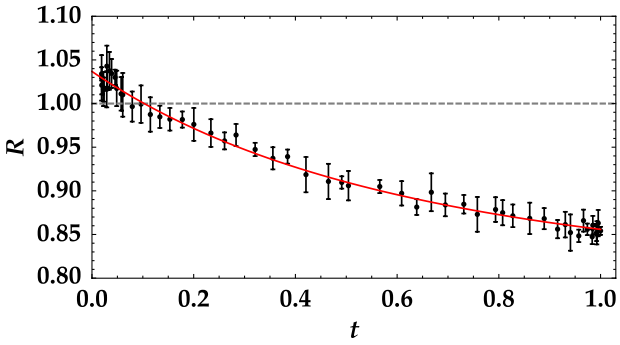

Fig. 3. Experimental values of R as a function of t. Black dots and error bars: experimental data; red line: theoretical fitting function in which η and $\langle m\rangle/\mu$ are the fitting parameters. In particular, we have $\eta = 0.144 \pm 0.001$ and $\langle m\rangle/\mu = 0.037 \pm 0.002$. The dashed gray line at $R = 1$ represents the boundary condition.

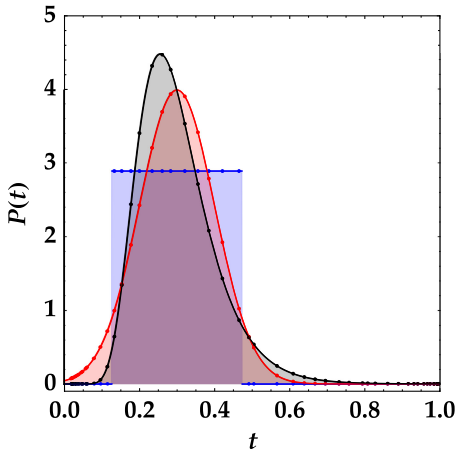

Fig. 4. Distributions of the transmission efficiency with mean value $t_0 = 0.3$ and standard deviation $\sigma = 0.1$: Uniform distribution (blue curve), Gaussian distribution (red curve), and log-normal distribution (black curve). The colored dots represent the experimental realizations of these distributions obtained by changing the transmission efficiency in steps.

detector through a multi-mode fiber with 600 μm core diameter. As to the detectors, we use two hybrid photodetectors (Model R10467U-40, Hamamatsu Photonics), whose outputs are amplified, synchronously integrated, and digitized. The imbalance between the two arms is obtained by inserting in arm 1 a half-wave plate (HWP) followed by a polarizing cube beam splitter. By rotating the HWP in steps of 2°, we are able to change the transmission efficiency of the arm from 0 to 1. For each angle, 50,000 acquisitions are performed.

By exploiting the self-consistent method extensively explained elsewhere [21,23], for each laser shot we determine the number of photons detected in the two arms. In particular, for each step of the HWP we calculate the mean number of detected photons. In arm 2 the mean value is fixed, i.e., $\langle m_2\rangle = 2.10 \pm 0.01$, while in arm 1 it varies from a maximum value, i.e., $\langle m_1\rangle_{\max} = 2.23 \pm 0.02$, down to $\langle m_1\rangle_{\min} = 0.042 \pm 0.001$. The transmittance efficiency t is determined as the ratio between the measured value of $\langle m_1\rangle$ and its maximum value, namely $t = \langle m_1\rangle/\langle m_1\rangle_{\max}$. Thus, $0.019 < t < 1$.

The experimental values of R as a function of the transmission efficiency t are shown in Fig. 3 as black dots and error bars. In the same figure we also show the theoretical fitting function (red curve) according to Eq. (4), in which η and $\langle m\rangle/\mu$ are considered as fitting parameters. The mean number of photons per mode obtained from the fit ($\langle m\rangle/\mu = 0.037 \pm 0.002$) proves that the generated TWB states are quite multi-mode and thus nonclassicality can be observed down to low values of t.

3. MODELING THE TRANSMISSION EFFICIENCY

In order to take into account a more realistic scenario, in which the transmission efficiency is described by a statistical distribution instead of a single value, in the following we study the behavior of R in three different cases: a uniform distribution, a Gaussian distribution, and a log-normal distribution of t. In Fig. 4, we present the three distributions $P(t)$ (colored lines) in the case in which all of them are characterized by the same mean value $t_0 = 0.3$ and the same standard deviation $\sigma = 0.1$. Superimposed to the analytical distributions there are their experimental realizations (colored dots), which are obtained by varying the transmission efficiency in steps (see the previous section). For all the three models, we investigate what happens to R for different mean values and standard deviations of the transmission efficiency. In this case, the expression in Eq. (2) must be averaged according to the probability distribution of t in the interval [0,1], namely,

$$R = \frac{\int_0^1 \mathrm{d}t\, P(t)\langle (m_1 - m_2)^2\rangle - \left(\int_0^1 dt\, P(t)\langle m_1 - m_2\rangle\right)^2}{\int_0^1 \mathrm{d}t\, P(t)(\langle m_1\rangle + \langle m_2\rangle)}. \tag{5}$$

For a multi-mode TWB state, this expression reduces to

$$R = 1 - \frac{2\eta\langle t\rangle}{(1+\langle t\rangle)} + \frac{\langle m\rangle}{\mu}\frac{(1-\langle t\rangle)^2}{(1+\langle t\rangle)} + \langle m\rangle\left(1+\frac{1}{\mu}\right)\frac{\sigma^2(t)}{(1+\langle t\rangle)}, \tag{6}$$

in which $\langle t\rangle$ and $\sigma^2(t)$ are the mean value and the variance of the generic distribution $P(t)$ evaluated in the interval [0,1]. Note that, in the case of a δ-distribution, which describes the situation in which t assumes specific values, Eq. (6) reduces to Eq. (4).

The direct comparison among the three distributions, as well as among the same distribution for different parameters, gives useful information about the role of the imbalance between the two correlated arms. Moreover, it also suggests which are the most critical parameters to keep under control.

A. Uniform Distribution

First of all, we deal with a transmission of t uniformly distributed. From the practical point of view, such a distribution corresponds to having a channel in which the transmission is progressively reduced from a maximum value down to a minimum one. In the case of a spectrally multi-mode TWB, the

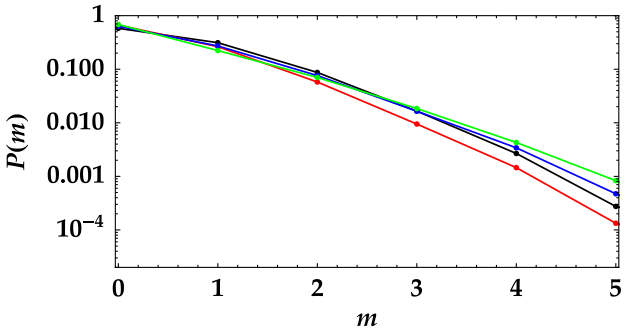

Fig. 5. Photon-number distributions, in logarithmic scale representation, of signal in arm 1 obtained by combining the experimental data according to a uniform distribution of the transmission efficiency with mean value $t_0 = 0.2$ and different standard deviations. The different colors correspond to $\sigma = 0.024$ (black), 0.053 (red), 0.102 (blue), and 0.144 (green).

uniform distribution can roughly describe the loss introduced by a narrow bandpass filter, which acts differently on the different spectral components. To obtain the effect of a uniform distribution with experimental data, we group together the data corresponding to the different transmission efficiencies. For each transmission efficiency t_i in the interval [0,1], we consider a number of data corresponding to the value of $P(t_i) \cdot 50{,}000$, in which 50,000 is the length of each dataset. This operation determines a modification of the photon-number statistics in arm 1. Indeed, some histograms, obtained by combining the data according to a uniform distribution with mean value $t_0 = 0.2$ and variable standard deviation, are shown in Fig. 5. The logarithmic scale is used to better emphasize the differences among the distributions. To evaluate the survival of nonclassicality, we group the experimental data by considering four choices of standard deviation and investigate the behavior of the noise reduction factor as a function of t_0. In particular, the experimental values of the standard deviation are $\sigma_{\text{exp}} = 0.024 \pm 0.004$, 0.053 ± 0.001, 0.102 ± 0.002, and 0.144 ± 0.002.

In Fig. 6 the data, shown as colored dots and error bars, are superimposed on the theoretical expectations (colored curves), calculated according to Eq. (6) by setting $\langle m \rangle = 2.1$ and leaving η and μ as fitting parameters. All the conditions in Fig. 6 display a threshold value of t_0 below which $R > 1$. In addition, we note that the nonclassicality criterion becomes stricter at increasing σ.

From the analysis above we can conclude that there are conditions under which even a low value of transmission efficiency still guarantees the observation of nonclassical correlations, provided the width of the transmission window is narrow enough. On the contrary, to preserve nonclassicality in the case of large values of σ, larger values of t_0 are required.

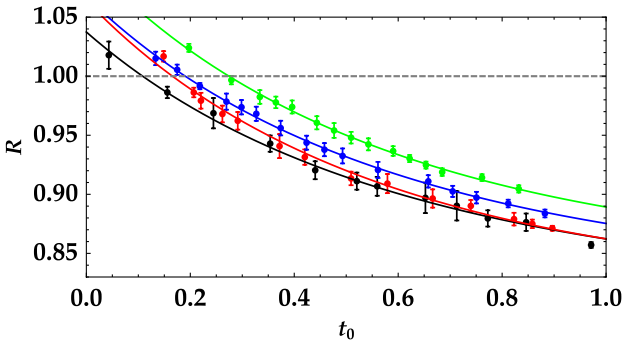

Fig. 6. Noise reduction factor R as a function of the mean value t_0 of the uniform distribution for $\sigma_{\text{exp}} = 0.024$ (black), 0.053 (red), 0.102 (blue), and 0.144 (green). Colored dots and error bars: experimental data; colored lines: theoretical expectations, in which the values of the fitting parameters are $\eta = 0.138$ and $\mu = 57.89$ for the black curve, $\eta = 0.141$ and $\mu = 36.93$ for the red curve, $\eta = 0.136$ and $\mu = 46.36$ for the blue curve, and $\eta = 0.133$ and $\mu = 39.21$ for the green curve. The dashed gray line at $R = 1$ represents the boundary condition.

B. Gaussian Distribution

As a second example, we consider a Gaussian distribution of t:

$$P_{\text{g}}(t) = \frac{1}{\sqrt{2\pi}\sigma} \exp\left[\frac{-(t - t_0)^2}{2\sigma^2}\right]. \tag{7}$$

At variance with the uniform distribution, a Gaussian one is smoother at the edges, thus being more suitable to mimic the effects of optical elements. Also in this case, we consider a set of distributions having different mean values, t_0, and different standard deviations, σ. As in the case of uniform distribution, we are interested in investigating the behavior of R as a function of t_0 for given values of σ. To this aim, we weight the experimental data already presented in the previous section according to Gaussian distributions. In particular, we set $\sigma = 0.08$, 0.10, 0.12, 0.15 and vary the mean value within the interval [0,1]. In Fig. 7 we show the experimental mean values of the distributions versus the expected ones, which are well aligned on the diagonal. We note that the theoretical values were obtained by considering the real range in which the transmission efficiency is varied, that is [0,1]. The values of the relative error, which is defined as $\sum_i^N |\langle t_i \rangle_{\text{exp}} - (t_0)_i| / [N \cdot (t_0)_i]$, N being the total number of data in each plot, are quite low. In more detail, for the datasets shown in Fig. 7 we get 0.006, 0.006, 0.006, and 0.007, respectively. The photon-number distributions, obtained by combining the data according to Gaussian distributions with $t_0 = 0.2$ and variable width (i.e., $\sigma = 0.08$, 0.10, 0.12, and

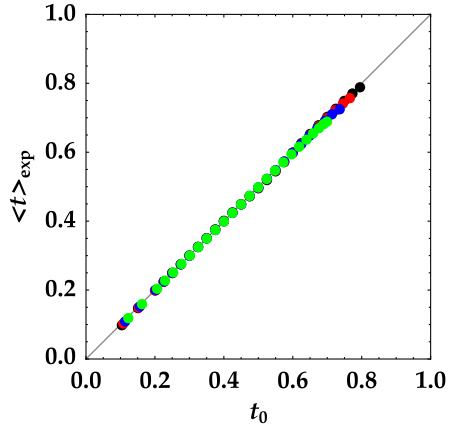

Fig. 7. Mean values of the Gaussian distributions obtained from the experimental data versus the theoretical ones. Black dots: $\sigma = 0.08$, red dots: $\sigma = 0.10$, blue dots: $\sigma = 0.12$, green dots: $\sigma = 0.15$. In the figure, the gray line indicates the diagonal on which the data should be superimposed.

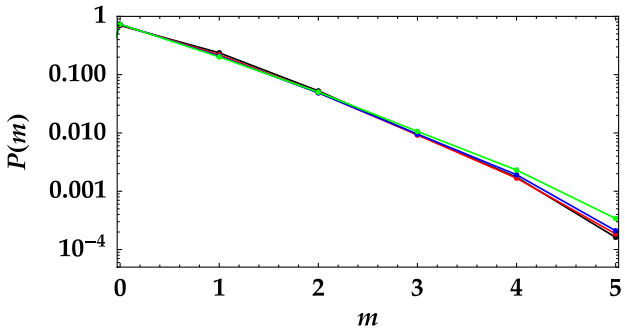

Fig. 8. Photon-number distributions, in logarithmic scale representation, obtained in arm 1 by combining the experimental data according to a Gaussian distribution of the transmission efficiency with $t_0 = 0.2$ and different standard deviations. The different colors correspond to $\sigma = 0.08$ (black), 0.10 (red), 0.12 (blue), and 0.15 (green).

0.15), are shown in Fig. 8. Note that the changes in the statistical properties can be appreciated only on a logarithmic scale. Nevertheless, the behavior of the noise reduction factor as a function of the mean value of t for given values of the standard deviations exhibits quite noticeable differences. Indeed, the larger the width of the distribution, the harder the observation of nonclassicality.

In Fig. 9, the colored dots correspond to the experimental values of R as a function of t_0, whereas the colored curves represent the theoretical expectations calculated according to Eq. (6), by setting $\langle m \rangle = 2.1$ and leaving η and μ as fitting parameters. Different colors correspond to different values of the standard deviation: black to $\sigma = 0.08$, red to 0.10, blue to 0.12, and green to 0.15. From the direct comparison between the data shown in Fig. 9 and those in Fig. 6, we can argue that preserving nonclassicality is slightly more critical when the transmission efficiency follows a Gaussian distribution instead of a uniform one. This behavior can be ascribed to the smoother shape of the Gaussian distribution.

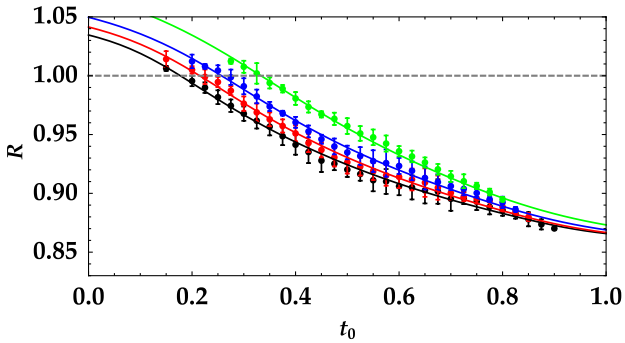

Fig. 9. Noise reduction factor R as a function of the mean value t_0 of the Gaussian distribution of the transmission efficiency for different values of the standard deviation (black symbols correspond to $\sigma = 0.08$, red ones to 0.10, blue ones to 0.12, and green ones to 0.15). Colored dots and error bars: experimental data; colored lines: theoretical expectations, in which the values of the fitting parameters are $\eta = 0.142$ and $\mu = 36.91$ for $\sigma = 0.08$, $\eta = 0.144$ and $\mu = 29.77$ for $\sigma = 0.10$, $\eta = 0.145$ and $\mu = 24.28$ for $\sigma = 0.12$, and $\eta = 0.147$ and $\mu = 17.28$ for $\sigma = 0.15$. The dashed gray line at $R = 1$ represents the boundary condition.

C. Log-Normal Distribution

As a third example we consider the log-normal distribution:

$$P_{\ln}(t) = \frac{1}{\sqrt{2\pi}\sigma_\xi t} \exp\left[\frac{-[-\xi + ln(t)]^2}{2\sigma_\xi^2}\right], \tag{8}$$

in which $\xi \in \Re$ is the location parameter and $\sigma_\xi > 0$ is the scale parameter. From these two factors it is possible to determine all the moments of the distribution, i.e., $\langle t^s \rangle = \exp[s\xi + s^2\sigma_\xi^2/2]$. In particular, we note that the mean value of t is $t_0 = \exp[\xi + \sigma_\xi^2/2]$, while the variance is $\sigma^2 = (\exp[2\xi + \sigma_\xi^2])(-1 + \exp[\sigma_\xi^2])$. This distribution is usually adopted for modeling atmospheric turbulence effects in the case of strong turbulence [15,17]. By following the same reasoning already used in the case of Gaussian distribution, hereafter we present the results obtained by grouping our data according to log-normal distributions. For the sake of clarity, in Fig. 10 we show some selected distributions with $t_0 = 0.3$ and $\sigma = 0.08, 0.11$, and 0.13.

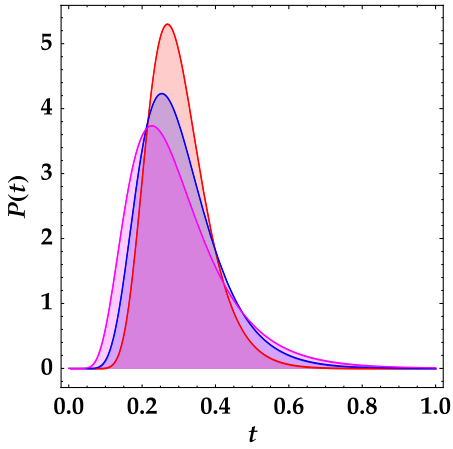

Fig. 10. Log-normal distributions of the transmission efficiency normalized to the area for $t_0 = 0.3$ and different standard deviations: $\sigma = 0.08$ (red), 0.11 (blue), 0.14 (magenta).

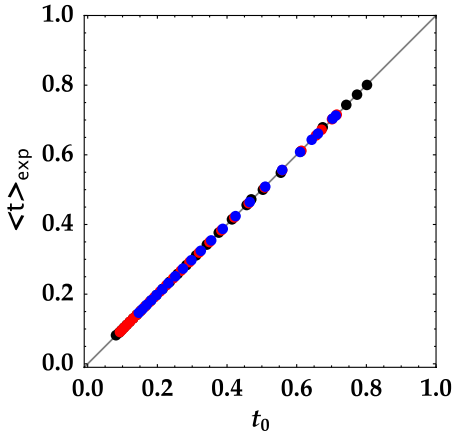

Fig. 11. Mean values of the log-normal distributions obtained from the experimental data versus the theoretical ones. Black dots: $\sigma = 0.08$, red dots: $\sigma = 0.11$, and blue dots: $\sigma = 0.14$. In the figure, the gray line indicates the diagonal on which the data should be superimposed.

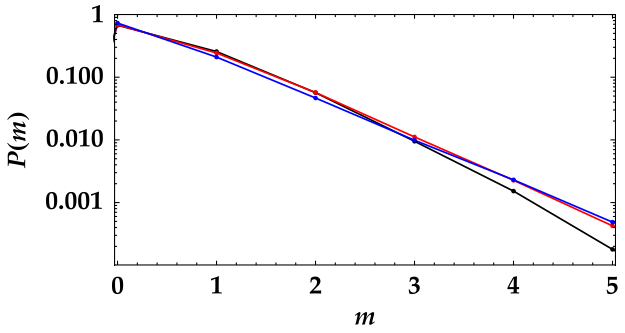

Fig. 12. Photon-number distributions, in logarithmic scale representation, obtained in arm 1 by combining the experimental data according to a log-normal distribution of the transmission efficiency with $t_0 = 0.2$ and different standard deviations. The different colors correspond to $\sigma = 0.08$ (black), 0.11 (red), and 0.14 (blue).

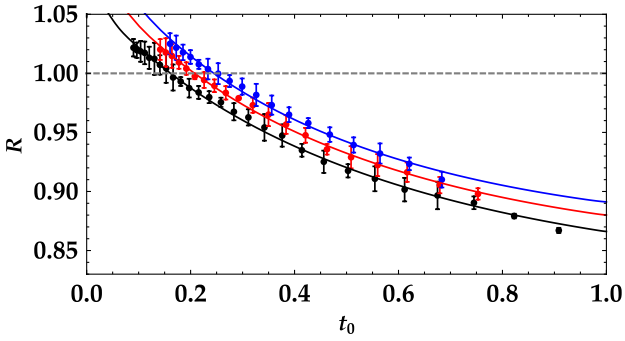

Fig. 13. Noise reduction factor R as a function of the mean value t_0 of the log-normal distribution of the transmission efficiency for different values of the standard deviation (black symbols correspond to $\sigma = 0.08$, red ones to 0.11, and blue ones to 0.14). Colored dots and error bars: experimental data; colored lines: theoretical expectations, in which the values of the fitting parameters are $\eta = 0.134$ and $\mu = 40.71$ for $\sigma = 0.08$, $\eta = 0.121$ and $\mu = 33.82$ for $\sigma = 0.11$, and $\eta = 0.110$ and $\mu = 30.92$ for $\sigma = 0.14$. The dashed gray line at $R = 1$ represents the boundary condition.

To make a fair comparison with the distributions presented in the previous sections, we investigate the behavior of R as a function of the mean value of t for fixed values of the standard deviation, by suitably varying both the scale value and the location parameter. In the panels of Fig. 11 we show the experimental values of $\langle t \rangle$ versus the theoretical ones for $\sigma = 0.08$, 0.11, and 0.14. The corresponding relative errors are equal to 0.002 and 0.002, and 0.001, respectively. Note that, like in the case of the Gaussian distribution, the theoretical expectations have been obtained by calculating the log-normal distribution in the range [0,1].

By grouping the experimental data according to the third kind of distribution for specific choices of σ, the photon-number statistics are slightly modified. For instance, in Fig. 12 we show the light statistics for $t_0 = 0.2$ and $\sigma = 0.08$ (black symbols), 0.11 (red symbols), and 0.14 (blue symbols). Like in the previous cases, the differences among the distributions are visible only on a logarithmic scale representation. In Fig. 13 we plot the experimental values of the noise reduction factor as a function of the mean values t_0 of the log-normal distribution for three different choices of σ, i.e., $\sigma = 0.08$, 0.11, and 0.14. All the data are well superimposed on the theoretical models, calculated according to Eq. (6), by setting $\langle m \rangle = 2.1$ and leaving η and μ as fitting parameters. Like the cases of uniform and Gaussian distributions of t, also the present case becomes critical at increasing values of σ. However, it seems that this third kind of distribution is slightly better for the observation of nonclassicality. In our opinion, such a behavior could be naïvely ascribed to the shape of the distribution. Indeed, the log-normal distribution has asymmetric tails, and extends more toward large values of t. Thus, the widening of the distribution is compensated by the inclusion of high values of transmittivity.

4. DISCUSSION AND CONCLUSIONS

In this paper, we have explored the survival of nonclassical correlations between the two parties of mesoscopic TWB states affected by a strong imbalance in the transmission efficiency. In particular, we have investigated the case in which the transmission efficiency t of one of the arms is varied from 0 to 1, while that of the other is kept fixed. To make the system more realistic, we also explored the situation in which the transmission efficiency is distributed according to some specific distributions. Since the change of the transmission efficiency was obtained in steps, we have evaluated the similarity of the distributions obtained from the data to the expected ones. In all cases, we have observed that nonclassicality is preserved even for small mean values of the transmission efficiency, provided the standard deviation is low enough. It came out that, among the distributions, the most critical is the Gaussian one, for which we noticed the largest dependence of the values of the noise reduction factor on the different choices of the standard deviation. In particular, the larger the distribution of the transmission efficiency, the harder the observation of nonclassical correlations. As a further perspective, it would be desirable to study the effects on TWB nonclassicality of an additional noise source instead of a variable amount of loss.

Acknowledgment. We thank Alberto Parola (University of Insubria) for fruitful suggestions.

REFERENCES

1. I. Marcikic, H. D. Riedmatten, W. Tittel, H. Zbinden, and N. Gisin, "Long-distance teleportation of qubits at telecommunication wavelengths," Nature **421**, 509–513 (2003).
2. R. Ursin, T. Jennewein, M. Aspelmeyer, R. Kaltenbaek, M. Lindenthal, P. Walther, and A. Zeilinger, "Communications: quantum teleportation across the Danube," Nature **430**, 849 (2004).
3. R. Ursin, F. Tiefenbacher, T. Schmitt-Manderbach, H. Weier, T. Scheidl, M. Lindenthal, B. Blauensteiner, T. Jennewein, J. Perdigues, P. Trojek, B. Ömer, M. Fürst, M. Meyenburg, J. Rarity, Z. Sodnik, C. Barbieri, H. Weinfurter, and A. Zeilinger, "Entanglement-based quantum communication over 144 km," Nat. Phys. **3**, 481–486 (2007).
4. Q. Zhang, H. Takesue, S. W. Nam, C. Langrock, X. Xie, B. Baek, M. M. Fejer, and Y. Yamamoto, "Distribution of time-energy entanglement over 100 km fiber using superconducting single-photon detectors," Opt. Express **16**, 5776–5781 (2008).
5. T. Scheidl, R. Ursin, A. Fedrizzi, S. Ramelow, X.-S. Ma, T. Herbst, R. Prevedel, L. Ratschbacher, J. Kofler, and T. Jennewein, "Feasibility

of 300 km quantum key distribution with entangled states," New J. Phys. **11**, 085002 (2009).
6. A. Fedrizzi, R. Ursin, T. Herbst, M. Nespoli, R. Prevedel, T. Scheidl, F. Tiefenbacher, T. Jennewein, and A. Zeilinger, "High-fidelity transmission of entanglement over a high-loss free-space channel," Nat. Phys. **5**, 389–392 (2009).
7. I. Capraro, A. Tomaello, A. Dall' Arche, F. Gerlin, R. Ursin, G. Vallone, and P. Villoresi, "Impact of turbulence in long range quantum and classical communications," Phys. Rev. Lett. **109**, 200502 (2012).
8. J. Yin, J.-G. Ren, H. Lu, Y. Cao, H.-L. Yong, Y.-P. Wu, C. Liu, S.-K. Liao, F. Zhou, Y. Jiang, X.-D. Cai, P. Xu, G.-S. Pan, J.-J. Jia, Y.-M. Huang, H. Yin, J.-Y. Wang, Y.-A. Chen, C.-Z. Peng, and J.-W. Pan, "Quantum teleportation and entanglement distribution over 100-kilometre free-space channels," Nature **488**, 185–188 (2012).
9. X.-S. Ma, T. Herbst, T. Scheidl, D. Wang, S. Kropatschek, W. Naylor, B. Wittmann, A. Mech, J. Kofler, E. Anisimova, V. Makarov, T. Jennewein, R. Ursin, and A. Zeilinger, "Quantum teleportation over 143 kilometres using active feed-forward," Nature **489**, 269–273 (2012).
10. C. Peuntinger, B. Heim, Ch. Müller, Ch. Gabriel, Ch. Marquardt, and G. Leuchs, "Distribution of squeezed states through an atmospheric channel," Phys. Rev. Lett. **113**, 060502 (2014).
11. G. Vallone, D. Dequal, M. Tomasin, F. Vedovato, M. Schiavon, V. Luceri, G. Bianco, and P. Villoresi, "Interference at the single photon level along satellite-ground channels," Phys. Rev. Lett. **116**, 253601 (2016).
12. L. Ji, J. Gao, A.-L. Yang, Z. Feng, X.-F. Lin, Z.-G. Li, and X.-M. Jin, "Towards quantum communications in free-space seawater," Opt. Express **25**, 19795–19806 (2017).
13. J. Yin, Y. Cao, Y.-H. Li, S.-K. Liao, L. Zhang, J.-G. Ren, W.-Q. Cai, W.-Y. Liu, B. Li, H. Dai, G.-B. Li, Q.-M. Lu, Y.-H. Gong, Y. Xu, S.-L. Li, F.-Z. Li, Y.-Y. Yin, Z.-Q. Jiang, M. Li, J.-J. Jia, G. Ren, D. He, Y.-L. Zhou, X.-X. Zhang, N. Wang, X. Chang, Z.-C. Zhu, N.-L. Liu, Y.-A. Chen, C.-Y. Lu, R. Shu, C.-Z. Peng, J.-Y. Wang, and J.-W. Pan, "Satellite-based entanglement distribution over 1200 kilometers," Science **356**, 1140–1144 (2017).
14. N. Gisin and R. Thew, "Quantum communication," Nat. Photonics **1**, 165–171 (2007).
15. D. Vasylyev, A. A. Semenov, and W. Vogel, "Atmospheric quantum channels with weak and strong turbulence," Phys. Rev. Lett. **117**, 090501 (2016).
16. D. Yu. Vasylyev, A. A. Semenov, and W. Vogel, "Toward global quantum communication: beam wandering preserves nonclassicality," Phys. Rev. Lett. **108**, 220501 (2012).
17. M. Bohmann, R. Kruse, J. Sperling, C. Silberhorn, and W. Vogel, "Probing free-space quantum channels with laboratory-based experiments," Phys. Rev. A **95**, 063801 (2017).
18. A. Allevi and M. Bondani, "Can nonclassical correlations survive in the presence of asymmetric lossy channels?" Eur. Phys. J. D **72**, 178 (2018).
19. A. De Pasquale, A. Mari, A. Porzio, and V. Giovannetti, "Amendable Gaussian channels: restoring entanglement via a unitary filter," Phys. Rev. A **87**, 062307 (2013).
20. A. Allevi, S. Olivares, and M. Bondani, "Measuring high-order photon-number correlations in experiments with multimode pulsed quantum states," Phys. Rev. A **85**, 063835 (2012).
21. A. Allevi and M. Bondani, "Nonlinear and quantum optical properties and applications of intense twin-beams," Adv. At. Mol. Opt. Phys. **66**, 49–110 (2017).
22. I. I. Arkhipov, J. Peřina, Jr., J. Peřina, and A. Miranowicz, "Comparative study of nonclassicality, entanglement, and dimensionality of multimode noisy twin beams," Phys. Rev. A **91**, 033837 (2015).
23. M. Bondani, A. Allevi, A. Agliati, and A. Andreoni, "Self-consistent characterization of light statistics," J. Mod. Opt. **56**, 226–231 (2009).